09

# Applicability of white light interferometers for measuring X-ray optical component roughness

© M.M. Barysheva,[1,2] N.I. Chkhalo,[1,2] Yu.A. Vainer,[1] M.V. Zorina,[1] M.S. Mikhailenko,[1] R.M. Smertin[1]

[1]Institute for Physics of Microstructures of the Russian Academy of Sciences,
603087 Afonino village, Kstov district, Nizhny Novgorod region, Russia
[2]Lobachevsky State University,
603022 Nizhny Novgorod, Russia
e-mail: mmbarysheva@ipmras.ru

*Received June 2, 2025*
*Revised June 2, 2025*
*Accepted June 2, 2025*

A supersmooth silicon wafer was used to demonstrate that modern white light interferometers provided reliable data even for high-precision wafers with subnanometer surface roughness. For validation of results obtained by mid-spatial frequency interference microscopy, PSD functions of the wafer surface measured using lenses with various magnifications, atomic force microscopy and synchrotron X-ray diffractometry were compared. Wafer roughness was measured at 0.8 nm in the spatial frequency range $1.5 \cdot 10^{-3} - 64\,\mu\text{m}^{-1}$.

**Keywords:** surface roughness, white light interferometry, spectral power density function, supersmooth surfaces, atomic force microscopy, diffuse X-ray scattering, mid-spatial frequencies.

DOI: 10.61011/TP.2025.10.62079.141-25

## Introduction

Surface roughness of X-ray mirrors and their wafers is a key property defining the utilization efficiency of a radiation source and resolution of devices that use these mirrors. For diffraction-quality X-ray mirrors, wafer roughness shall be controlled within the lateral dimension range from 1 nm to 1 mm, whereby the roughnesses with lateral dimensions from $1\,\mu\text{m} - 1$ to mm affect the mirror resolution to the greatest extent. Requirements for these roughnesses are at the level of 1–2 Å [1]. It should be considered that wafers generally have a curved shape. Atomic force microscopy ( AFM) and diffuse X-ray scattering (DXRS) are most widely used and reliable roughness measurement techniques. However, they have some limitations. AFM — a long-wavelength boundary of lateral dimensions due to scanner nonlinearity at $20-40\,\mu$m. DXRS — examination of curved surfaces is impossible, workpiece dimension limitations, errors introduced by the damaged layer during surface correction by ion etching. In recent years, this problem is solved by using white light interferometers (WLI) [2]. However, some works indicate that the method does well only for relatively rough surfaces [3,4]. For atomically-smooth wafers, the power spectral density (PSD) functions of roughness restored using the measurement data obtained using the Zygo and Talysurf CCI 2000 interferometers didn't overlap with the AFM and DXRS data in their operating spatial frequency range intersection regions. Whilst they remained almost the same for various samples. This may be caused by recording equipment noise, reference surface quality, aberrations of the detecting section of an optical system, because the sampling and reference fronts propagate through the system with inclination relative to each other, i.e. their paths are slightly shifted. Thus, when measuring atomically-smooth surfaces, the interferometer actually measured not only the surface itself, but also optical system noise and aberrations.

At the same time, complete refusal from the interference microscopy would be quite painful: it allows quick scanning of large areas and is well suited for examining smooth texture, i.e. surface irregularities with typical sizes from $1\,\mu\text{m} - 10$ to mm. Therefore, this work brings us back to the problem of using white light interferometry for measuring atomically-smooth surfaces represented by a silicon wafer using the SuperView W1 WLI. Evaluation of measurement adequacy uses the same principle — overlapping of roughness PSD functions measured by the WLI, AFM and DXRS techniques in the sampling range intersection region. Diffuse scattering is treated as an „ab initio" method. DXRS utilization limitations in examining surface roughness are reviewed in detail in a number of studies, for example, [5–8].

In contrast to [3], this study investigates synchrotron radiation scattering indicatrices for extending the measured spatial frequency range. Experiments were performed at the „FAZA" station, Kurchatov Synchrotron Research Center [9–11]. Findings for only one sample are given in this work, which is attributed to a limited access to the synchrotron infrastructure. However, similar examinations of other samples using a laboratory diffractometer fully confirm the given data at least for a spatial frequency range from $0.025\,\mu\text{m}^{-1}$ and higher, suggesting that the data given in this work have much in common.

## 1. Experimental sample preparation

A wafer made of single crystal silicon (001), $145 \times 30 \times 30$ mm, was used as an experimental sample. The sample was cut from a silicon ingot. Grinding and polishing were performed on the ZPD-350 triple-spindle machine by deep grinding and polishing followed by chemical-mechanical polishing. For the grinding stage, carbide-silicon polishing powders with abrasive grain sizes of 40, 28 and 10 $\mu$m, respectively, and metal grinders were used. For mechanical polishing, a pitch polisher (SP 5) and water suspension of Apoline cerium oxide micropowder with a grain size of $0.5-1\,\mu$m were used.

For chemical-mechanical polishing, an alkaline suspension of silicon oxide micropowder with a grain size smaller than 100 nm was used. Suede cloth was used as a polisher. A manufacturing process of single-crystal silicon wafers for electronics was actually followed [12]. Chemical and mechanical polishing was completed when roughness measured using the AFM technique reached its minimum and didn't change any longer.

Before each measurement, wafer surfaces were chemically cleaned in a solution of potassium dichromate in sulfuric acid followed by thorough washing in deionized water.

## 2. WLI technique

Interferometric optical techniques are widely used for surface roughness measurement due to their high (nanometer) precision, non-contact sensing and quick scanning of large areas. Modern interferometers such as white light or phase shifting ones produce 3D texture maps and allow automatic calculation of standard roughness parameters. These techniques are applicable to various materials, including metals, polymers and semiconductors, though require a sufficient surface reflectance. Thus, interferometry combines high resolution, measurement rate and absence of mechanical impact making it one of the most effective micro- and nanoroughness evaluation techniques.

High-coherence interferometry and low-coherence interferometry are distinguished. However, for supersmooth surface roughness measurement, high-coherence interferometry faces several fundamental limitations:

1) $2\pi$-ambiguity problem — phase measurements are repeated with $\lambda/2$ period, thus, making ambiguous determination of the absolute height impossible when there are sudden drops exceeding the half-wavelength;

2) spurious interference effects — high laser light coherence induces false fringe patterns from internal optical components, dust particles and scattered light that considerably distort measurements [13];

3) multiscattering effect — repeated light reflection from various irregularities on rough surfaces produces artefacts in the fringe pattern;

4) limited spatial resolution — a typical pixel size of $\sim 0.1$ mm, which corresponds to $\sim 0.005\,\mu\text{m}^{-1}$ in the wavenumber space, is insufficient for in-depth study of a small-scale microtexture.

Low-coherence WLI is free from these disadvantages [2,4,14]. A broadband source with a small coherence length ($1-5\,\mu$m) is used to determine unambiguously the interference signal envelope maximum, minimize the spurious reflection effect and effectively deal with surfaces with various degrees of roughness.

Interferometric surface examination technique is based on the analysis of a fringe pattern induced by interaction between coherent light beams from the reference and sampling interferometer arms [15]. For WLI, the broadband radiation source forms a beam that is separated into two ones: the first beam is reflected from a reference mirror (reference beam), and the second beam is reflected from the surface to be measured (sampling beam). Interference occurs only when optical paths coincide with accuracy up to the source coherence length that generally equal to several micrometers. 3D surface profile is measured by vertical scanning (Z scanning), when the fringe pattern envelope maximum is recorded for each image point. Further data processing allows creating a subnanometer-resolution height map (up to 0.1 nm vertically), whilst the horizontal resolution is limited by a diffraction limit ($\sim \lambda$). Advantages of the WLI technique include the ability to measure objects with low reflectance, significant height drops (from nanometers to millimeters) and complex microtexture, thus, making the technique indispensable for quality control of optical components, semiconductor structures and micro-electromechanical systems (MEMS). However, the measurement accuracy may decrease if there are vibrations or when examining multilayer structures that require additional reflections to be considered.

For the purpose of this study, roughness in a spatial frequency range of $\nu \in [10^{-3} - 1]\,\mu\text{m}^{-1}$ was measured using the SuperView W1 WLI (Chotest Technology Inc, China). Interferometer diagram is shown in Figure 1. WLI includes broadband light source *4*, collimating lens *9*, beam splitter *3*, interference objective (combining an objective lens, built-in beam splitter and reference mirror) on piezoactuator *6*, and focusing lens *2* and CCD matrix *1* arranged in series.

The principle of work of an interferometer is illustrated by a beam corresponding to one surface point (Figure 1, *a*): collimating light beam from source *4* strikes top beam splitter *3* and is directed to interference objective *6*. When travelling through objective lens *5*, the beam strikes bottom beam splitter *3*, where it is divided into two beams: the reference beam is reflected from reference mirror *8* inside the interference objective, and the sampling beam is focused by the objective lens onto surface to be measured *7*, both beams interfere after reflection. Fringe pattern in the beam splitter plane is projected onto CCD detector *1* using lens *2*. Due to a short white light coherence length, interference is observed only when the optical path lengths are close to each other (path difference$\leq$ coherence length). To achieve

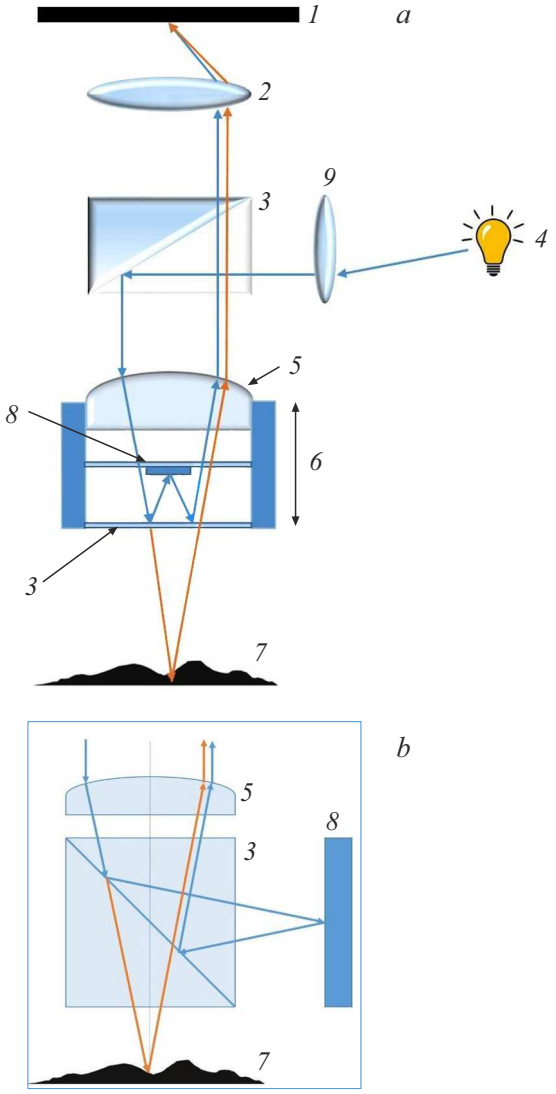


**Figure 1.** *a* — Diagram of the Mirau interferometer (*b* — Michelson interferometer). *1* — detector; *2* — objective lens; *3* — beam splitter; *4* — light source; *5* — interference objective lens; *6* — piezoactuator; *7* — surface to be measured; *8* — reference plane; *9* — collimating lens.

the optical path equality, a piezoactuator is used to move the interference objective vertically. The detector measures light intensity, when the interferometric objective travels vertically, and finds the fringe pattern envelope maximum.

In the SuperView W1 microscope, a range available for movement in the sample plane is $140 \times 100$ mm with lateral resolution in the order of 1 $\mu$m. The maximum vertical travel range is 100 mm, vertical resolution is 0.1 nm. The device is used to examine any types of surfaces (convex, concave, saddle-like) and to calculate curvature radii in two directions starting from $R = 1$ mm to infinity with a reflectivity from 0.05 % to 100 %. Firmware provides surface measurements using the Mirau objectives with various magnification $\times 10$, $\times 20$ and $\times 50$ and, respectively, with various fields of view: $980 \times 980\,\mu$m, $480 \times 480\,\mu$m and $196 \times 196\,\mu$m.

**Table 1.** Standard deviations for each objective

| Objective | Standard deviation, nm |
|---|---|
| $\times 5$ | 0.07 |
| $\times 10$ | 0.06 |
| $\times 20$ | 0.03 |
| $\times 50$ | 0.16 |

Advantages of the Mirau objective include a compact design (all in one objective) and high stability with respect to vibrations because it has a short reference arm and rigid integral structure where all critical components are fixed in a common housing. However, it should be considered that such objective is unsuitable for transparent samples because false reflections are possible, and also has a limited sampling range due to a fixed reference arm.

A $\times 5$ objective with a $1960 \times 1960\,\mu$m field of view is a Michelson objective shown in Figure 1, *b*. The Michelson interferometer has reference surface *8* in another position: due to an increase in the field of view, the reference mirror shall have a larger diameter, therefore compact configuration as for the Mirau objective turns out to be a technically challenging problem. Such design allows using transparent samples, however it is more sensitive to vibrations and reference mirror slope with respect to the optical axis.

Before starting the measurements, a set of preparations was performed to ensure the maximum data accuracy. At the first stage, a successive approximation method was used to determine the optimum number of frame averaging events to suppress effectively noise components without significant measurement time increase. Statistical analysis showed that averaging over 10 frames provided an optimum relation between accuracy and performance for the employed objectives, which is confirmed by standard deviation calculations for each of them as given below. Sampling was performed from 1 to 100 averages of one frame. Table 1 shows standard deviations for objectives with different magnification. The given data reflects roughness measurement stability for each objective. It can be seen that in all cases, except for $\times 50$, a subangstrom roughness measurement repeatability is achieved.

Prior to measurements, the sample was placed on a vibration insulated interferometer table and held for 1.5 h to achieve a thermal balance in the system and stabilize possible thermomechanical drifts. Measurement procedure included repeated surface scanning followed by data averaging and mathematical processing.

Since the test sample is flat, data processing was limited to a slope correction by subtracting the approximated plane. The obtained frame with dimensions $L \times L$ was saved in the form of a square height matrix $z(x, y)$ with dimensions equal to $1024 \times 1024$ points. Then the table of surface heights is used to calculate the power spectral density

(PSD) function. The PSD function is a powerful tool for surface analysis due to its ability to characterize in detail the spatial distribution of irregularities. In contrast to traditional roughness parameters such as PV (peak-to-valley) and RMS (root-mean-square), PSD allows separating the contribution of various spatial scales to the resulting roughness. This is important because multiscale spatial defects affect the image in different ways when it is formed in X-ray optics [1].

For a square surface area with dimensions of $N \times N$ points and sample spacing $L/N$ on both axes, a $2D$ PSD function ($\mathrm{PSD}_{2D}$) may be calculated through the fast Fourier transform of the height matrix $z(x, y)$ to provide full description of spatial frequency characteristics of the surface:

$$\mathrm{PSD}_{2D}(v_x, v_y) = \frac{1}{N^2}\frac{L^2}{N^2}\,|\mathrm{FFT}_{2D}[z(x, y)]|^2, \qquad (1)$$

$$v_x = \frac{2\pi n}{L}, \quad v_y = \frac{2\pi m}{L}, \quad n, m = -\frac{N}{2}, \ldots, \frac{N}{2} - 1.$$

A 1D PSD function ($\mathrm{PSD}_{1D}$), being an important particular case, may be derived by averaging $\mathrm{PSD}_{2D}$ over angles for isotropic surfaces to ensure preservation of full information concerning irregularity distribution or through forward Fourier transform of individual linear profiles, which is especially useful for fast comparative analysis:

$$\mathrm{PDS}_{1D}(v_x) = \frac{1}{N_v}\,\langle \mathrm{PSD}_{2D}(v_x, v_y)\rangle\Big|_{v=\sqrt{v_x^2+v_y^2}},$$

where $N_v$ is the number of dots in a frequency ring with the radius $v$, along which averaging is performed, or

$$\mathrm{PSD}_{1D}(v_x) = \frac{1}{N}\frac{L}{N}\,|\mathrm{FFT}_{1D}[z(x)]|^2, \qquad (2)$$

$$v_x = \frac{2\pi n}{L}, \quad n = -\frac{N}{2}, \ldots, \frac{N}{2} - 1.$$

Theoretical relation between these representations is based on the fact that $\mathrm{PSD}_{1D}$ is a two-dimensional spectrum projection, which preserves the information concerning the dependence of roughness on the spatial scale, but loses surface anisotropy data. Note that both approaches require strict normalization to the area of the examined segment (for $\mathrm{PSD}_{2D}$) or to the length of the examined segment (for $\mathrm{PSD}_{1D}$) to ensure correct quantitative comparisons between different measurements. Additional normalization by a factor of $1/N$ or $1/N^2$ provides independence of the PSD function on the number of points in a frame: $N$ influences only the number of spatial frequencies, for which the PSD function was determined. Keeping in mind the fast comparison of measurements with each other and with the diffuse X-ray scattering data, the 1D PSD functions will be used hereinafter.

## 3. AFM and DXRS

Alternative techniques used to confirm the data obtained by white-light interferometry and refining the technique applicability range for supersmooth surfaces are described below.

Wafer roughness was measured on the Ntegra Prima atomic-force microscope bench (NT-MDT), Zelenograd) to study the roughness of large parts. The bench is placed in a separate room provided with sound-insulation, temperature and humidity control. Independent foundation and passive vibration protection in the form of spring suspension ensure low noise level during scanning [3]. Roughness was measured using the TipsNano NSG10 probe with a probe tip curvature radius of 10 nm. This technique also allows reconstruction of the test sample surface height map. Mathematically, this approach is equivalent to white light fringe pattern processing.

Preliminary processing of these atomic-force measurements included topographic slope correction by subtracting the reference plane, then further surface analysis was performed using the above-mentioned technique for white light interference microscopy data. The $\mathrm{PSD}_{1D}$ function was calculated according to (2) along the scanning lines and then averaged over all frame lines: though the wafer surface is isotropic in itself and has no any surface texture, when proceeding to supersmooth surfaces, PSD functions calculated along and across the probe motion during scanning get to be slightly different due to the measurement artefacts induced by probe movement between lines. However, these variations were less than 10 % of the measured quantity, and this effect was neglected in this study.

The scanning area size was determined by trade-off between sampling time, hardware limitations and required resolution. The number of sampling points was $256 \times 256$: doubling of the number of scanning points results in a fourfold growth of the measurement time, whilst actually only one additional point is added to the PSD function. Frame dimensions were $40 \times 40$ and $2 \times 2\,\mu$m. When the frame dimensions exceed $40 \times 40\,\mu$m, a growing piezoscanner nonlinearity starts having its effect. The lower limit ($2 \times 2\,\mu$m) is defined by artefacts induced by the finite curvature radius of the sensing probe.

The second technique, with which the findings were compared, is diffuse scattering of hard X-rays ($\lambda \sim 0.1$ nm). The technique deals with a grazing incidence geometry where the incoming light with the wavelength $\lambda$ strikes the sample at a shallow angle $\theta_0$ close to a critical total external reflection angle and is scattered at angles $\theta$, $\varphi$. The geometry of the experiment is shown in Figure 2.

At the perturbation theory approximation, the magnitude of roughness may provide a relation between the 2D light scattering indicatrix $\Phi(\theta, \varphi)$ and the surface roughness 2D PSD function $\mathrm{PSD}_{2D}(\nu)$, which was initially done in the optical range [14] and later was widely used in the X-ray range [5–7]:

$$\Phi(\theta, \varphi) = \frac{|\pi(1-\varepsilon)t(\theta_0)t(\theta)|^2}{\lambda^4 \sin(\theta_0)}\,\mathrm{PSD}_{2D}(\nu), \qquad (3)$$

$$\nu = \frac{1}{\lambda}\,\{\cos\theta\cos\varphi - \cos\theta_0; \cos\theta\sin\varphi\},$$

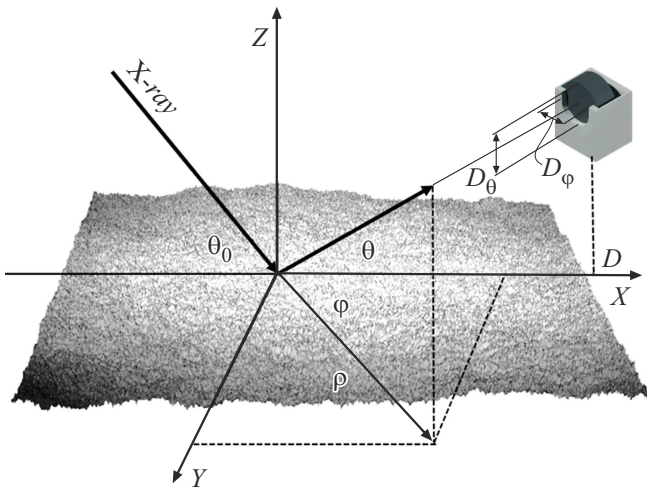


**Figure 2.** Geometry of the experiment for investigating diffuse X-ray scattering by a rough surface.

where $\varepsilon$ is the dielectric permittivity of the wafer material, $\theta_0$ is the grazing angle of incidence, $\theta$ is the scattering angle in the plane of incidence, $\varphi$ is the scattering angle in the perpendicular plane; $t(\theta)$, $t(\theta_0)$ are the Fresnel transmission coefficients for the corresponding angles.

If $a$ is the correlation roughness length, then the angular dimensions of the scattering diagram may be approximately estimated as $\delta\theta \sim \lambda/(\pi \cdot a \cdot \sin\theta)$ and $\delta\varphi\lambda/\pi a$, i.e. $\delta\varphi \ll \delta\theta$ at angles close to the critical angle, which means that the $\Phi(\theta, \phi)$ scattering diagram is strongly elongated along $\theta$ and allows proceeding from 2D distribution of$\Phi(\theta, \phi)$ to 1D distribution $\Pi(\theta) = \int_{-\infty}^{\infty} \Phi(\theta, \phi)$:

$$\Pi(\theta) = \frac{|\pi(1-\varepsilon)t(\theta_0)t(\theta)|^2}{2\lambda^3 \sin(\theta_0)\sqrt{\cos\theta_0 \cos\theta}} \mathrm{PSD}_{1D}(\nu), \qquad (4)$$

$$\nu = \frac{1}{\lambda} |\cos\theta - \cos\theta_0|.$$

For scattering signal recording in real practice, the DXRS experiment uses a detector that is placed at the distance $D$ from the sample and has dimensions $D_\theta$ (in the light incidence plane) and $D_\varphi$ (in the perpendicular plane) — defined by the entrance slit dimensions. To proceed to (4), a broad slit $D_\varphi/D \gg \delta\varphi$ in the plane perpendicular to the incidence plane is sufficient. Intensity recorded by the detector will be defined as $I(\theta) = \Pi(\theta)\mathrm{D}_\theta/l$. Thus, the diffuse scattering intensity $I(\theta)$ at the angle$\theta$ to the surface is unambiguously defined by scattering on irregularities with a particular spatial frequency $\nu$.

The maximum detectable frequency $\nu_{\max}$, according to (4), theoretically doesn't exceed $2/\lambda$, and is practically defined by the maximum scattering angle $\theta_{\max}$, for which a signal can be still detected, i.e. depends on the instrument's dynamic range. Consequently, the minimum lateral dimension of irregularities detected by this technique is $\sim \lambda/\sin\theta_{\max}$. The minimum frequency $\nu_{\min}$ ($\nu_{\min} = 0$ according to (4)) is limited by the capability of separating the contributions of the specularly reflected and diffuse components to a detected signal, i.e. by the angular resolution of the experimental system, which corresponds to the maximum detectable spatial roughness scales: irregularities with large lateral dimensions deflect the scattered light weaker, therefore the signal scattered by such irregularities still enters the detector in a position corresponding to the specular reflection (equivalent to a diffraction grating). To separate the signal induced by scattering on surface irregularities, contribution of the specular component is subtracted from the whole signal. Then, $\mathrm{PSD}_{1D}(\nu)$ is calculated using the experimental geometrical parameters, material's optical constants and analytical relation (3) by the obtained $I(\theta)$. Optical constants of the material and Fresnel transmission ratios are calculated by fitting the experimentally measured X-ray specular reflection curve.

The described model and its fundamental limitations are discussed in detail in [5]. When deriving equation (4), no additional limitations were imposed on the roughness characteristics, the statistical distribution of irregularities and correlation function. The only requirement is the applicability of perturbation theory, which for a fractal surface model (inverse power law decay of the PSD function) may be written as

$$\frac{2\pi}{\lambda}\sigma\theta_c \ll 1, \qquad (5)$$

where $\sigma$ corresponds to a RMS deviation, $\theta_c$ is the critical angle of total external reflection, $\theta_0 \cong \theta_c$. For X-ray radiation with $\lambda \cong 0.1$ nm and $\theta_c \sim 0.1°$, condition (5) is fulfilled for surfaces with roughness $\leq 1-2$ nm. For such surfaces, the DXRS technique may be considered as an ab initio method, i.e. as a reference method with respect to AFM and WLI.

Another factor limiting the DXRS applicability is X-ray scattering on bulk irregularities. This effect was first described in [15] and then studied in detail in [8]. These studies proposed a technique to identify the contribution of scattering from a wafer and, thus, to avoid erroneous interpretation of experimental data.

Diffuse X-ray scattering by rough wafers was studied at the FAZA station of Kurchatov Synchrotron Radiation Source. For the synchrotron source, 12.05 keV radiation ($\lambda \approx 1.03$ Å) and a test signal intensity of$\sim 10^7$ photons/s were used. Scattered radiation was recorded by the xHuber 9910 detector placed 1050 mm from the sample, with a 100 $\mu$m vertical slit in front of it. Exposure time was varied within $1-30$ s depending on the signal intensity, and slit and conical collimators were used to minimize background scattering.

Thus, for comparative surface quality analysis of various samples, their power spectral density (PSD) functions will be compared in a corresponding spatial frequency range. At the same time, for quantitative evaluation, the effective roughness $\sigma_{\mathrm{eff}}$ is more suitable and is defined as an integral

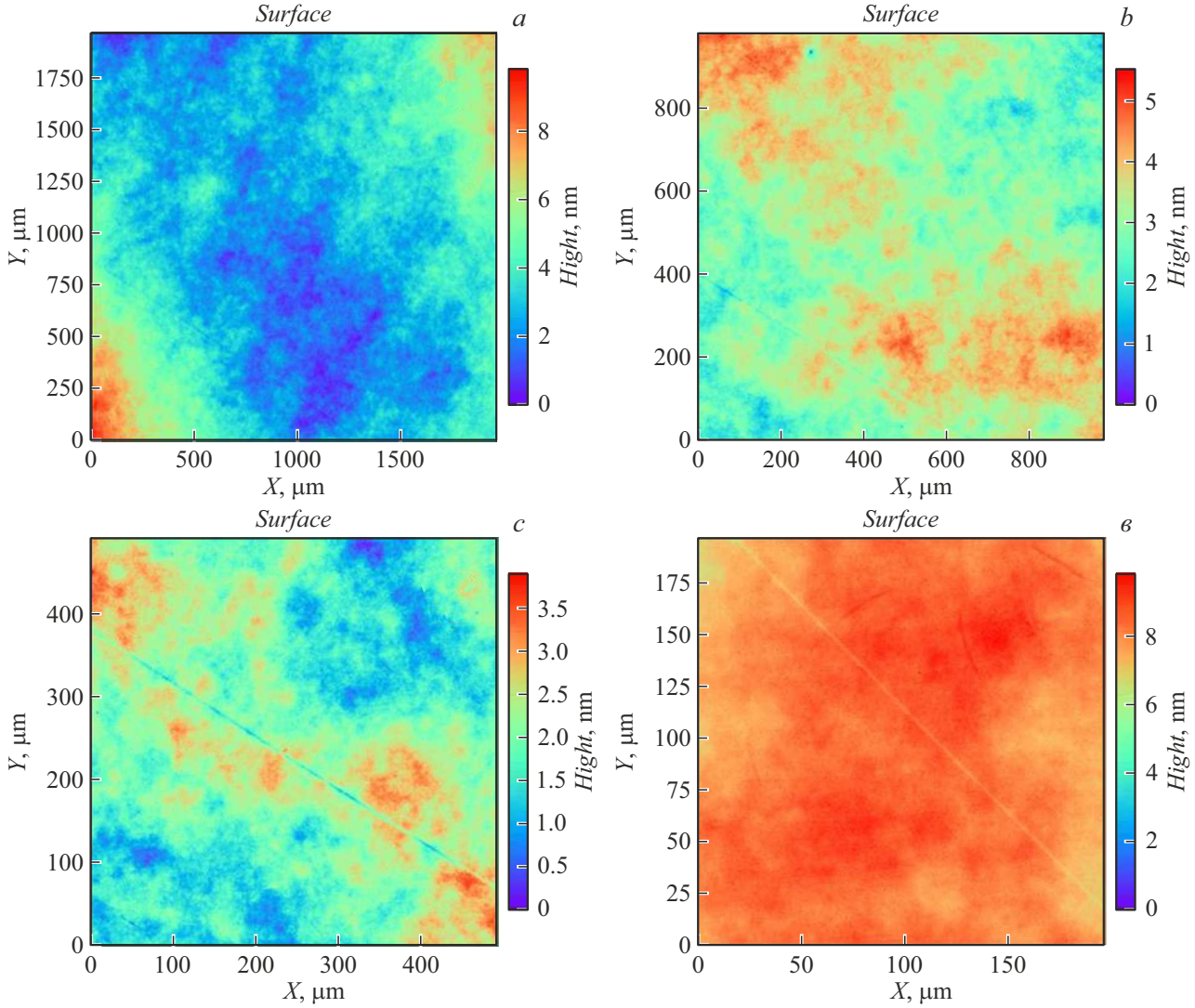


**Figure 3.** Surface maps of a supersmooth single crystal silicon wafer measured using the white light interference microscope with various lens magnifications: ×5 (*a*), ×10 (*b*), ×20 (*c*), ×50 (*d*).

microtexture characteristic in the specified frequency range:

$$\sigma_{\text{eff}} = \left( \int_{\upsilon_{\min}}^{\upsilon_{\max}} \text{PSD}_{1D}(\upsilon) d\upsilon \right)^{1/2}, \qquad (6)$$

where $\upsilon_{\min}$ and $\upsilon_{\max}$ define the boundaries of the length scale of interest. In the limit case, when integration covers all available spatial frequencies, the value thus calculated coincides with the common RMS parameter that characterizes the deviation of surface heights:

$$\text{RMS} = \left( \int_{0}^{\infty} \text{PSD}_{1D}(\upsilon) d\upsilon \right)^{1/2}. \qquad (7)$$

Comparison between (6) and (7) explains the difference in roughness values obtained using different techniques when describing a surface by a single parameter — RMS roughness height: each of them defines the effective roughness in its frequency range. Power spectral density (PSD) used for complete description of surface makes it possible to avoid such inconsistencies because PSD accounts for irregularity distribution over all spatial frequencies.

## 4. Findings and discussion

Figures 3 and 4 show the surface maps of the polished supersmooth silicon wafer, sample Si0325, obtained from the AFM and white light interference microscopy data. The frames are typical for high quality surfaces free of contamination.

The diffuse scattering measurements obtained using the synchrotron source are shown in Figure 5. Figure 5, *a* shows a normalized scattering indicatrix obtained with $\theta = 0.1413°$. As shown in Figure 5, *a*, the dynamic intensity range was more than 7 orders of magnitude, which allows going ahead into a higher spatial frequency region compared

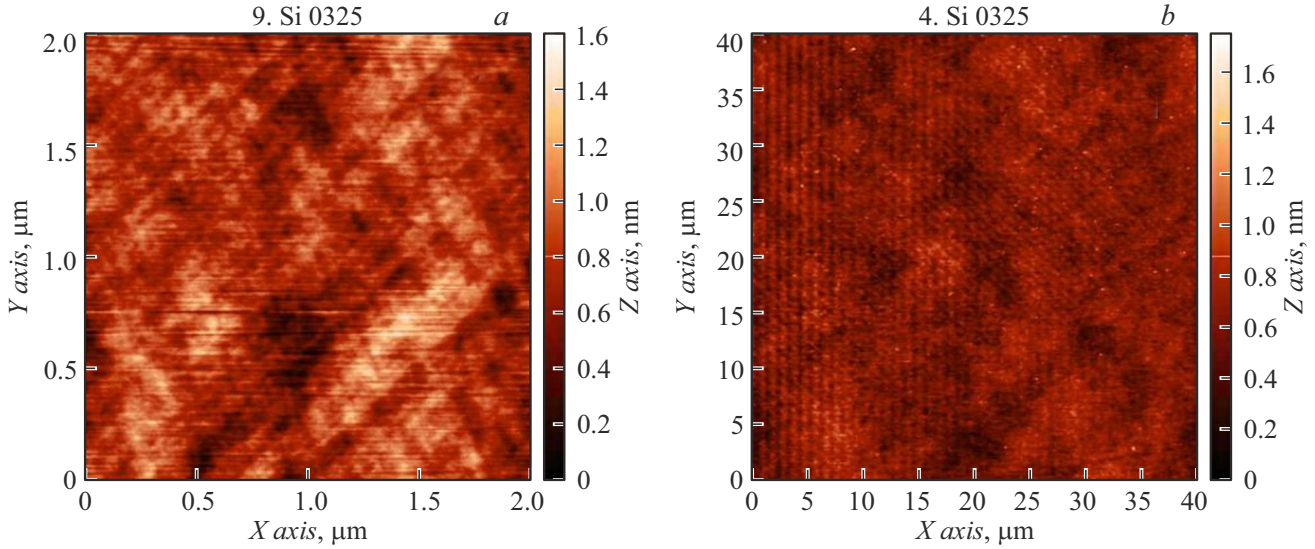


**Figure 4.** Surface maps of a polished supersmooth silicon wafer measured using AFM: $2 \times 2\,\mu$m ($a$) and $40 \times 40\,\mu$m ($b$).

**Table 2.** Effective roughnesses of the polished supersmooth silicon wafer measured using various qualification techniques

| Technique | Characteristics | $[\nu_{\min};\ \nu_{\max}],\ \mu\text{m}^{-1}$ | $\sigma_{\text{eff}}$, nm |
|---|---|---|---|
| AFM | frame $40 \times 40\,\mu$m | $[2.5 \cdot 10^{-2};\ 3.17]$ | 0.14 |
| | frame $2 \times 2\,\mu$m | $[0.5; 63.5]$ | 0.11 |
| WLI | lens $\times 5$ | $[1.5 \cdot 10^{-3}; 0.26]$ | 0.73 |
| | lens $\times 10$ | $[2 \cdot 10^{-3}; 0.52]$ | 0.49 |
| | lens $\times 20$ | $[4 \cdot 10^{-3}; 1.04]$ | 0.43 |
| | lens $\times 50$ | $[1 \cdot 10^{-2}; 2.6]$ | 0.29 |
| XRDS | $E = 2.05$ keV, $\lambda \approx 1.03$ Å, $\theta_0 = 0.1413°$ | $[2 \cdot 10^{-3}; 2.7]$ | 0.55 |

with laboratory diffractometers. Figure 5, $b$ shows a test beam intensity distribution without a sample. Measurement was performed by angular detector scanning.

The most significant issue is in correct consideration of the specularly reflected intensity, and it is this consideration that defines the long-wavelength boundary of the DXRS technique. First, the sample has a limited size, therefore some incident beam „wings“ pass the sample by without contributing to the reflected or scattered signal intensity. In Figure 5, $c$, curve $I_0 * R$ (red squares) corresponds to the reflected component of the test beam, and the difference of the scattering indicatrix and test beam angular distribution is also shown (the calculation included the reflected beam inversion with respect to the incident beam). For $\theta = 0.1413°$ and a sample size of 145 mm, this means a reflected beam projection in the detector plane $\cong 0.36$ mm, which is comparable with a detector slit size of 0.1 mm. Artefact of this calculation is a discontinuous change on the curve corresponding to the scattering signal with the mirror component (blue triangles) subtracted from the change. The second issue associated with studying a long sample is in the fact that components scatted from different parts of the sample strike the detector at different angles, which correspond to the scattering angle range $\Delta\theta = \theta \cdot S/D$, where $S$ is the sample size and $D$ is the sample-detector distance [7]. For example, for the given silicon sample, we get $\Delta\theta \cong 0.02°$ at $\theta = 0.15°$. Correct consideration would smooth down the non-physical jump on the scattering curve, however, such technique is not available to us at this point. Moreover, there is also spurious scattering from slit edges, sample chamber walls, and components within the source, which also cannot be reliably considered in calculations.

PSD functions calculated on the basis of the given data are shown in Figure 6, $a$. Table 2 shows the effective roughnesses obtained for each of the techniques in accordance with (6). PSD curves corresponding to various measurement techniques demonstrate a similar slope and overlap in the mid-spatial frequency region. The jump on the PSD function measured by diffuse scattering is an artefact of the reflected signal subtraction procedure, has no

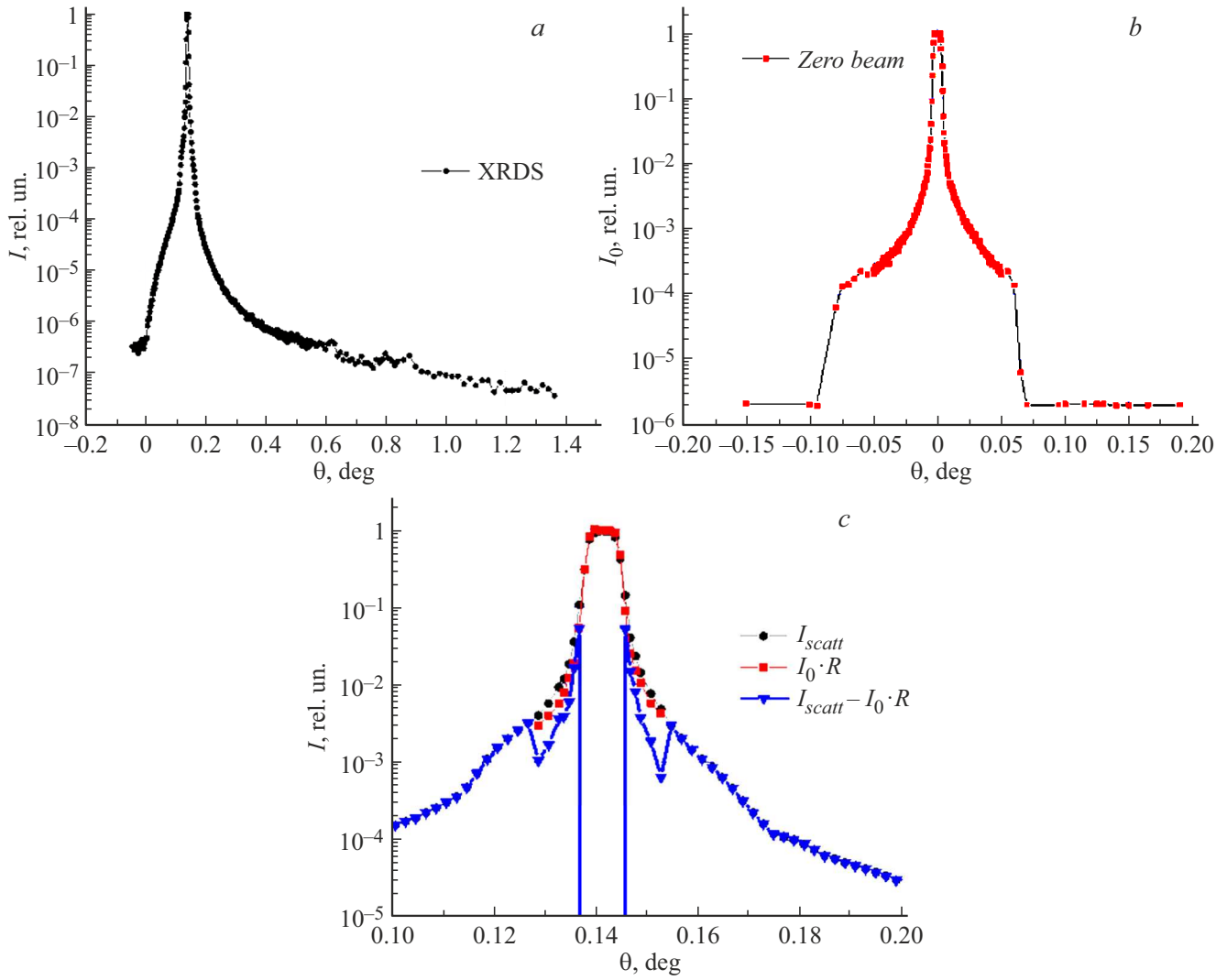


**Figure 5.** Diffuse scattering indicatrix of the polished supersmooth silicon wafer ($a$), test beam intensity distribution ($b$) and calculation of the difference of the scattering indicatrix and test beam angular distribution ($c$). The angle of radiation incidence onto the sample is $\theta = 0.1413^\circ$.

physical sense and is smoothed in real practice. However, the diffuse scattering method covers the spatial frequency range from $2 \cdot 10^{-3}$ to $2.7\,\mu\text{m}^{-1}$, i.e. three orders of magnitude, which exceeds the capabilities of a laboratory diffractometer by an order of magnitude [3,8] and makes it possible to use the method for evaluating correctness of WLI measurements.

In turn, PSD functions obtained by the interference microscopy technique also well coincide with each other for various mid-frequency range lenses, but demonstrate sudden signal drop at high spatial frequencies, with the „failure“ point shifted depending on the lens magnification. This phenomenon is caused by limitations of the system's optical resolution that is defined by the numerical aperture (NA) of a lens and light source wavelength. First, this technique, just like any other optical technique, obeys the Rayleigh criterion, according to which the minimum resolution is $\sim \lambda/(2\text{NA})$. When the lens magnification is increased, NA of the lens grows and shifts the threshold detectable frequency towards higher frequencies, which explains the dependence of the PSD failure point on the magnification. The finite pixel size of the camera also has an effect: even when the optical system is capable of resolving small irregularities on its own, detection of these irregularities requires sufficient discretization. When the pixel size is too large, high-frequency texture components are „averaged“, thus, leading to PSD underestimation.

If the „optical“ PSD function edges sagging in the high-frequency region are dropped and only the frequency range $1.5 \cdot 10^{-3} - 64\,\mu\text{m}^{-1}$ is used, the wafer's PSD function averaged over various measurements may be approximated by three linear (logarithmic) segments with different slope as shown in Figure 6, *b*. Thus, the surface is multifractal or multiscale. The type of surface may be described by the

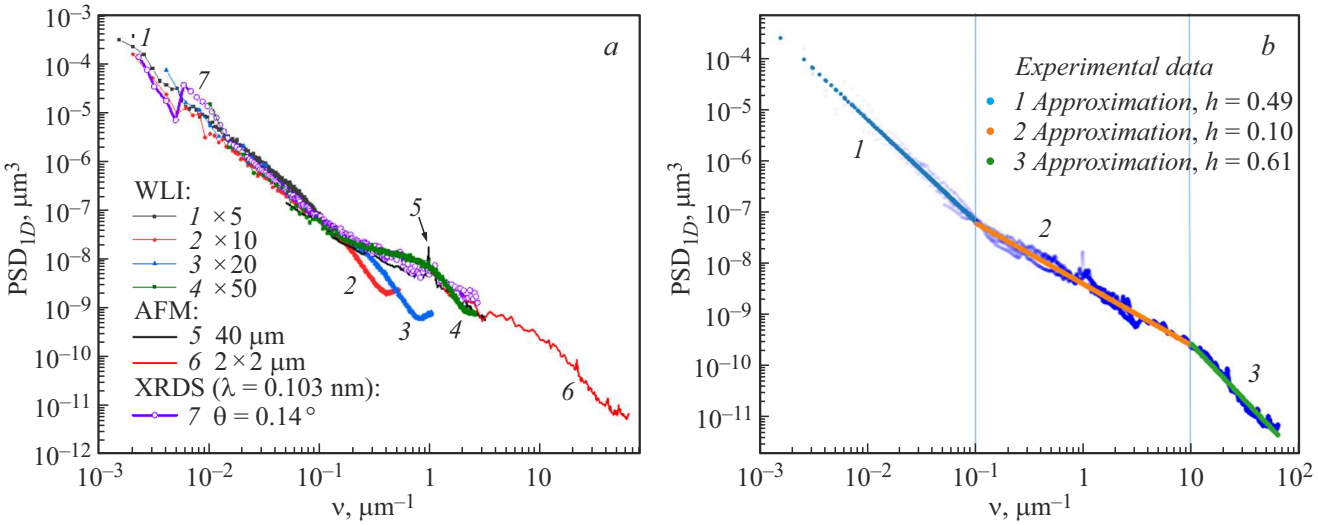


**Figure 6.** PSD-functions of the polished supersmooth silicon wafer measured using the AFM, white light interference microscopy and diffuse X-ray scattering techniques (*a*) and the averaged final PSD function (*b*).

Hurst exponent $h$ that characterizes the PSD function as [7]:

$$\mathrm{PSD}_{1D} \cong \frac{C}{\nu^{2h+1}}, \quad 0 < h < 1. \tag{8}$$

Values of $h$ for each segment are shown in Figure 6, *b*.

Total effective roughness calculated using the approximated data over $1.5 \cdot 10^{-3} - 64\,\mu\mathrm{m}^{-1}$ was $\sigma_{\mathrm{eff}} = 0.8$ nm, which corresponds to wafers of sufficiently high quality.

## Conclusions

The study demonstrates that modern surface roughness analysis techniques: AFM, white light interference microscopy and diffuse X-ray scattering produce consistent results in the overlapping spatial frequency range. Modern WLIs provide valid data even for high-precision wafers with subnanometer surface roughness, which removes the previous doubts concerning the reliability of this technique. It is shown that even one lens provides reliable results in the mid-spatial frequency region, and several lenses with different magnifications expand the range of interest. The obtained results are very important for metrology of surfaces with ultra-small irregularities.

### Funding

The study was performed under state assignment FFUF-2024-0022 with respect to metrology and under grant № 21-72-20108-P of Russian Science Foundation with respect to experimental data interpreting.

### Conflict of interest

The authors declare no conflict of interest.

## References

[1] U. Dinger, F. Eisert, H. Lasser, M. Mayer, A. Seifert, G. Seitz, S. Stacklies, F.-J. Stickel, M. Weiser. Proc SPIE, **4146**, 35 (2000). DOI: 10.1117/12.406674
[2] S. Iles, J. Nelson. SPIE, **11175**, 246 (2019). DOI: 10.1117/12.2536683
[3] M.M. Barysheva, Y.A. Vainer, B.A. Gribkov, M.V. Zorina, A.E. Pestov, D.N. Rogachev, N.N. Salashchenko, N.I. Chkhalo. Bull. Russ. Academy Sci.: Phys., **75** (1), 67 (2011). DOI: 10.3103/S1062873811010059
[4] J. Chen, T. Sun, J. Wang. SPIE, **7656**, 583 (2010). DOI: 10.1117/12.863268
[5] V.E. Asadchikov, I.V. Kozhevnikov, Y.S. Krivonosov. Crystallography Reports, **48** (5), 836 (2003). DOI: 10.1134/1.1612604
[6] I.V. Kozhevnikov, V.E. Asadchikov, I.N. Bukreeva, A. Duparre, Yu.S. Krivonosov, C. Morawe, V.I. Ostashev, M.V. Pyatakhin, E. Ziegler. Proc. SPIE, **4099**, 267 (2000). DOI: 10.1117/12.405809
[7] V.E. Asadchikov, I.V. Kozhevnikov, Yu.S. Krivonosov, R. Mercier, T.H. Metzger, C. Morawe, E. Ziegler. Nucl. Instrum. Methods Phys. Res. A, **530**, 575 (2004). DOI: 10.1016/j.nima.2004.04.216
[8] M.M. Barysheva, N.I. Chkhalo, M.N. Drozdov, M.S. Mikhailenko, A.E. Pestov, N.N. Salashchenko, Yu.A. Vainer, P.A. Yunin, M.V. Zorina. J. X-Ray Sci. Technol., **27**, 857 (2019). DOI: 10.3233/XST-190495
[9] *Kurchatov Center for Synchrotron Radiation and Nanotechnology. PHASE beamline*. http://kcsni.nrcki.ru/pages/main/sync/beamlines/phaza/index.shtml
[10] A.A. Chernyshov, A.A. Veligzhanin, Y.V. Zubavichus. Nucl. Instrum. Methods Phys. Res. A, **603**, 95 (2009). DOI: 10.1016/j.nima.2008.12.167
[11] R. Senin, M. Borisov, E. Mukhamedzhanov, M. Kovalchuk. Acta Crystallogr. A, **73**, C862 (2017). DOI: 10.1107/S2053273317094028

[12] *TELSTV. Silicon wafers*.
http://www.telstv.ru/?page=en_silicon_wafers
[13] E.V. Petrakov, N.I. Chkhalo, A.K. Chernyshev, E.I. Glushkov. Opt. Eng., **63**, 114104 (2024).
DOI: 10.1117/1.OE.63.11.114104
[14] S.C.H. Thian, W. Feng, Y.S. Wong, J.Y.H. Fuh, H.T. Loh, K.H. Tee, Y. Tang, L. Lu. J. Phys.: Conf. Ser., **48**, 1435 (2006).
DOI: 10.1088/1742-6596/48/1/265
[15] R.K. Leach, L. Brown, X. Jiang, R. Blunt, M. Conroy, D. Mauger. *Guide to the measurement of smooth surface topography using coherence scanning interferometry. Measurement Good Practice Guide N 108* (National Physical Laboratory, Teddington, 2008),
http://eprintspublications.npl.co.uk/id/eprint/4099

*Translated by E.Ilinskaya*